


Nature of protected zero-energy states in Penrose quasicrystals

Ezra Day-Roberts ^{1,*}, Rafael M. Fernandes,¹ and Alex Kamenev^{1,2}

¹*School of Physics and Astronomy, University of Minnesota, Minneapolis, Minnesota 55455, USA*

²*William I. Fine Theoretical Physics Institute, University of Minnesota, Minneapolis, Minnesota 55455, USA*



(Received 6 May 2020; accepted 27 July 2020; published 20 August 2020)

The electronic spectrum of the Penrose rhombus quasicrystal exhibits a macroscopic fraction of exactly degenerate zero-energy states. In contrast to other bipartite quasicrystals, such as the kite-and-dart one, these zero-energy states cannot be attributed to a global mismatch Δn between the number of sites in the two sublattices that form the quasicrystal. Here, we argue that these zero-energy states are instead related to a *local* mismatch $\Delta n(\mathbf{r})$. Although $\Delta n(\mathbf{r})$ averages to 0, its staggered average over self-organized domains gives the correct number of zero-energy states. Physically, the local mismatch is related to a hidden structure of nested self-similar domains that support the zero-energy states. This allows us to develop a real-space renormalization-group scheme, which yields the scaling law for the fraction of zero-energy states, Z , versus the size of their support domain, N , as $Z \propto N^{-\eta}$ with $\eta = 1 - \ln 2/2 \ln \tau \approx 0.2798$ (where τ is the golden ratio). It also reproduces the known total fraction of zero-energy states, $81 - 50\tau \approx 0.0983$. We also show that the exact degeneracy of these states is protected against a wide variety of local perturbations, such as irregular or random hopping amplitudes, magnetic field, and random dilution of the lattice. We attribute this robustness to the hidden domain structure.

DOI: [10.1103/PhysRevB.102.064210](https://doi.org/10.1103/PhysRevB.102.064210)

I. INTRODUCTION

Quasicrystals were first discovered in 1982 by Shechtman *et al.* [1] in Al alloys. Within a short time, many other quasiperiodic crystals were discovered [2–4] including, eventually, a naturally occurring AlCuFe quasicrystal [5]. More recent work has focused on connecting quasicrystals with other novel phenomena such as topological states [6–9], non-Fermi-liquid behavior [10–13], superconductivity [14–17], and quantum criticality [18,19]. Synthetic quasicrystals were also recently created by arranging CO molecules on a Cu(111) surface with the aid of scanning tunneling microscopy [20].

Quasicrystals are known to display unusual properties in their density of states (DOS). All one-dimensional (1D) quasicrystals have a DOS that is only nonzero on a set of measure 0 [21,22]. The simplest 2D quasicrystals, which are built as Cartesian products of 1D quasicrystals, have densities of states that are related to those of their 1D counterparts [23,24]. On the other hand, the DOSs of intrinsic 2D and 3D quasicrystals can be rather different, displaying a sharp suppression at the Fermi level or a macroscopic number of zero-energy states [25–28].

In this paper, we focus on the nearest-neighbor tight-binding model on the Penrose rhombus lattice, which is known to display a macroscopic number of zero-energy states. (Although the term lattice is sometimes restricted to periodic structures, we use it to refer to both periodic and quasiperiodic structures here.) Several properties of these zero-energy states are well understood, including their fraction in the thermodynamic limit, $f = 81 - 50\tau \approx 9.8\%$, where $\tau = (\sqrt{5} + 1)/2$ is the golden ratio [29–31]. However, other properties are

not as clear, such as their microscopic origin and their stability against perturbations. Indeed, in nearest-neighbor tight-binding models on bipartite lattices, such as the Penrose lattice, zero-energy states can be trivially generated if the number of sites on the two sublattices, which we refer to as A and B , are not the same. In other words, there is a global mismatch $\Delta n \equiv n_A - n_B \neq 0$, implying the existence of a number of zero-energy states equal to $|\Delta n|$. This is precisely the case in the bipartite quasicrystal known as the Penrose kite-and-dart lattice, whose sublattice site mismatch gives rise to $\approx 10\%$ of zero-energy states. This is of course by no means limited to quasicrystals; for instance, the dice lattice has one third of its eigenstates at zero energy, reflecting the sublattice mismatch in each unit cell.

In the case of the Penrose rhombus lattice, however, there is no global mismatch in the thermodynamic limit, $\Delta n = 0$. This raises an important question about the nature of the zero-energy states. To address this issue, in this paper we introduce the concept of a *local* sublattice mismatch, $\Delta n(\mathbf{r})$. The key point is that, even though the average $\langle \Delta n(\mathbf{r}) \rangle$ is 0, the staggered average $\langle (-1)^{S_r} \Delta n(\mathbf{r}) \rangle$, in which $\Delta n(\mathbf{r})$ changes sign across certain regions denoted S_r , can be nonzero. The situation is analogous to an antiferromagnet: while the average magnetization vanishes, the average staggered magnetization is finite.

However, in contrast to an antiferromagnet, where the magnetization changes sign at the atomic length scale, the local mismatch $\Delta n(\mathbf{r})$ changes sign at much larger scales in the Penrose lattice. This is illustrated in Fig. 1, which shows the spatial variation of $\Delta n(\mathbf{r})$ for a Penrose lattice with about 4500 sites. In the red (blue) “domains,” the local sublattice mismatch is such that $n_A > n_B$ ($n_A < n_B$). Defining a staggered $\Delta n(\mathbf{r})$ by changing its sign in the blue domains compared to the red domains yields a finite number that

*dayro001@umn.edu

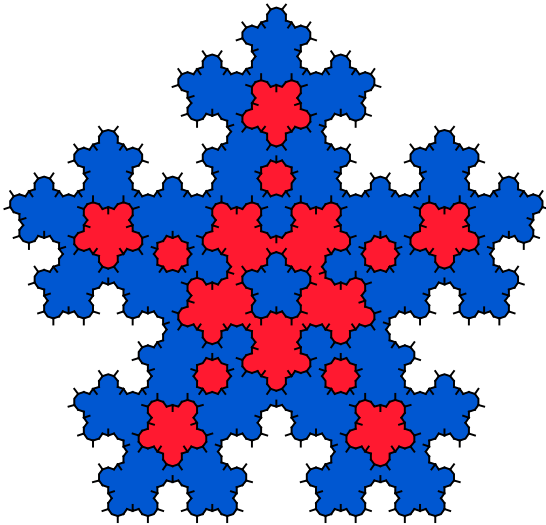


FIG. 1. A section of approximately 4500 sites of the Penrose rhombus lattice divided into domains showing the nesting of subdomains. In the red (blue) domains, the local sublattice mismatch is such that the A (B) sublattice has more sites than the B (A) sublattice. The domain walls connect sites belonging to different sublattices.

coincides with the number of zero-energy states. Interestingly, a recent investigation of the classical dimer model on the Penrose lattice found a result that resembles ours, namely, that the Penrose lattice supports a cluster structure with charge-alternating monomers, despite the fact that the Penrose lattice itself is globally charge neutral [32].

The connection between the staggered $\Delta n(\mathbf{r})$ and the zero-energy states can be made more transparent by considering the excluded sites (or forbidden sites, as they were originally called in Ref. [30]), i.e., sites for which the zero-energy states wave functions vanish. While inside the red domains the excluded sites are all in the A sublattice, in the blue domains they switch to the B sublattice. The domain walls (called strings in Ref. [30]) therefore connect excluded sites that belong to opposite sublattices.

We emphasize that this hidden geometric structure of the zero-energy states was noted in several previous works [14,30–33]. One of our main points here is to connect this structure to a staggered local mismatch $\Delta n(\mathbf{r})$ that spontaneously forms in the Penrose lattice. This geometric structure protects the zero-energy states from any perturbation that does not disrupt the large-scale nearest-neighbor structure. This includes, as previously found, a perpendicular magnetic field [33]. More generally, we demonstrate robustness against random nearest-neighbor hopping amplitudes and single-site vacancies. Even the addition of further hopping terms that break the bipartite symmetry, like next-nearest-neighbors (NNNs), only reduces the number of zero energy states linearly in the number of NNN hopping amplitudes.

The domain structure of the local mismatch $\Delta n(\mathbf{r})$, combined with the inflation properties of the Penrose lattice, also allows us to derive a recursive equation for the increase in the staggered mismatch as a function of the Penrose lattice generation. The structure of such a recursive relation resembles a real-space renormalization-group (RG) flow. Previous

works have applied the real-space RG technique to compute numerous quantities, such as solutions to the Ising model [34,35], the local density of states [36–38], and ground-state wave functions [39,40] for various quasicrystals including the Penrose lattice. Here, however, our goal is to determine the staggered local mismatch. We solve the flow equations to find the staggered mismatch in the infinite lattice limit. We find that the total number of staggered mismatched sites corresponds to a fraction $f = 81 - 50\tau \approx 0.0983$ of sites [31], showing that all zero-energy states in the Penrose lattice originate from this local mismatch structure. Using the real-space RG, we also find a scaling law $Z \propto N^{-\eta}$ that relates the fraction of zero-energy states, Z , to the size of their support domain, N . Our calculations give an exponent $\eta = 1 - \ln 2 / \ln(1 + \tau) \approx 0.2798$.

The paper is organized as follows. Section II contrasts the nature of the zero-energy states and of the global sublattice mismatch in two different Penrose quasicrystals, the kite-and-dart lattice and the rhombus lattice, and introduces the domain structure of the local mismatch in the rhombus lattice. Section III discusses the robustness of the zero-energy states against various perturbations as well as the spatial structure of the zero-energy states. Section IV uses the inflation property of the Penrose lattice to derive a real-space RG-like approach to determine the number of zero-energy states by exploiting its connection to the number of locally mismatched sublattice sites. Section V concludes the paper by discussing possible topological aspects of the zero-energy states. Appendices A, B, C, and D contain details about the derivation of the RG-like recursive relations.

II. PHENOMENOLOGY OF ZERO-ENERGY STATES IN QUASICRYSTALS

We consider tight-binding Hamiltonians defined on 2D quasicrystal lattices with zero on-site energies and nearest-neighbor hopping. Such Hamiltonians are numerically

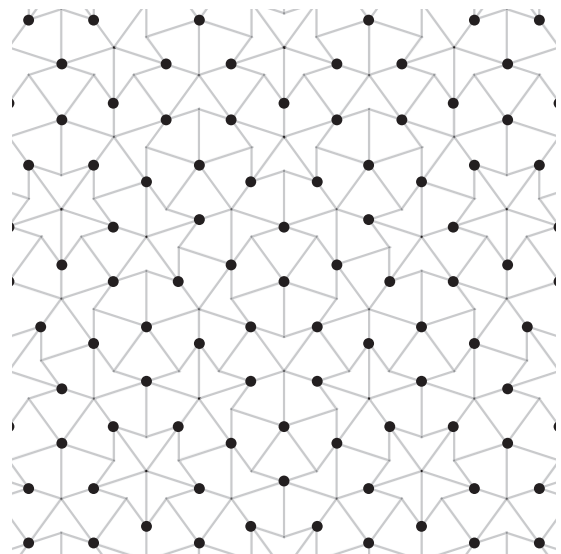


FIG. 2. Kite-and-dart lattice. Sites with *no* amplitude of *any* of the zero-energy states are represented by the black dots. Note that all marked sites belong to one sublattice.

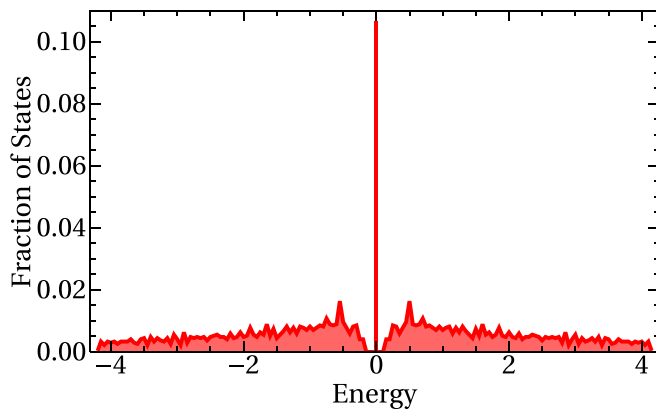


FIG. 3. Density of states for the kite-and-dart lattice. The DOS is symmetric about 0 and has a macroscopic number (~10%) of exactly zero-energy states.

diagonalized on lattices containing up to 11 000 sites. Below we summarize our findings for the kite-and-dart and rhombus lattices. It is important to stress that both these lattices are *bipartite*, with all sites belonging to either the *A* or the *B* sublattice and nearest-neighbor hopping operating solely between them.

A. The kite-and-dart lattice

Figure 2 shows a section of the kite-and-dart lattice. It is a quasicrystal with a fivefold rotational symmetry. The corresponding DOS is shown in Fig. 3, where a large peak of zero-energy states is clearly visible.

For this lattice the number of zero-energy states is entirely explained by the mismatch in the number of sites of the two sublattices, as listed in Table I. As expected for these zero-energy states, the amplitude of their wave functions is nonzero only on the majority sublattice. If the Hamiltonian is written in the sublattice basis, it takes the form of a block off-diagonal matrix:

$$\hat{H} = \begin{pmatrix} 0 & G \\ G^T & 0 \end{pmatrix}. \quad (1)$$

If the two sublattices have different numbers of sites, G has more columns than rows and so must have a null space at least as large as the difference between the sizes of the two sublattices. So there must be a vector(s) \vec{x} such that $G\vec{x} = 0$. Each of these corresponds to an eigenstate, $\psi_0 = (0, \vec{x})^T$, of Hamiltonian \hat{H} with the zero eigenvalue, $\hat{H}\psi_0 = 0$. Thus the

TABLE I. Numbers of zero-energy states and lattice mismatch in kite-and-dart lattices. The number of zero-energy states is completely explained by the (global) sublattice mismatch.

No. of sites	No. of zero-energy states	(Global) mismatch
166	24	24
411	41	41
1046	104	104
2686	286	286
6951	739	739

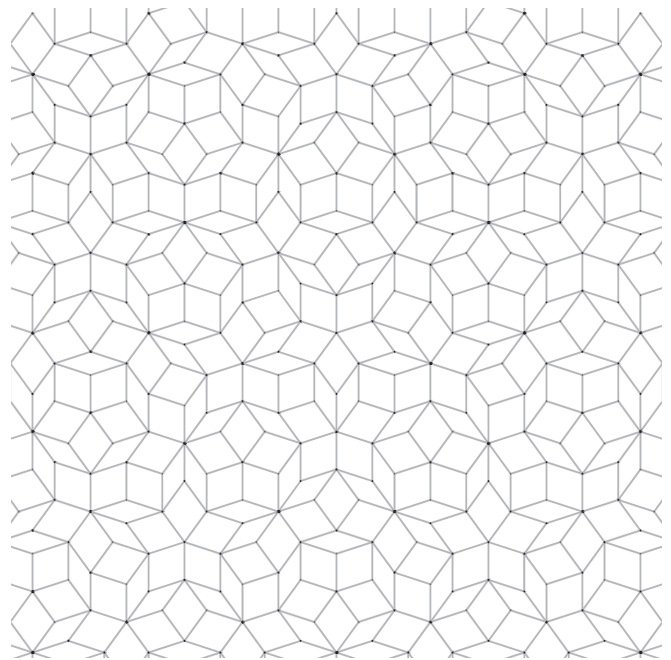


FIG. 4. The rhombus tiling is bipartite and has fivefold symmetry.

zero-energy eigenstates have amplitudes only on the majority sublattice and *no* amplitude on the minority sublattice. In Fig. 2 the sites that have *no* amplitude are represented by black dots, which indeed span the minority sublattice. Here the mismatch between the two global sublattices, Δn , exactly accounts for the ~10% of all the states having zero energy.

This situation is to some extent similar to, e.g., the dice lattice, which is bipartite with three sites per unit cell. Two sites belong to the majority and one to the minority sublattice. The mismatch is the third of all the sites and thus one third of all the states are at exactly zero energy (the so-called flat band). The difference is, of course, that the quasicrystal is not translationally invariant and the states are not labeled by the quasimomentum.

B. The rhombus lattice

The Penrose rhombus lattice is displayed in Fig. 4 and its DOS is shown in Fig. 5. Similarly to the kite-and-dart lattice, there is about 10% exactly zero-energy states. However, in this case this number cannot be explained by the mismatch between the two sublattices. As shown in Fig. 6 (see global mismatch line) the global relative sublattice mismatch Δn goes to 0, while the fraction of the zero-energy states saturates to a constant upon an increase in the lattice size.

To clarify the origin of the zero-energy states, we again mark all sites for which the wave function of the zero-energy states vanishes (we call them excluded sites), shown in Fig. 7. Unlike the kite-and-dart lattice, the excluded sites do not occupy a single sublattice. They are shown in red if they belong to the *A* sublattice and in blue if they belong to *B*. One notes that the two colors segregate into domains with well-defined boundaries, which run between alternating red and blue excluded sites (bold links in Fig. 7). Specifically, if all the bold links are cut, the lattice segregates into

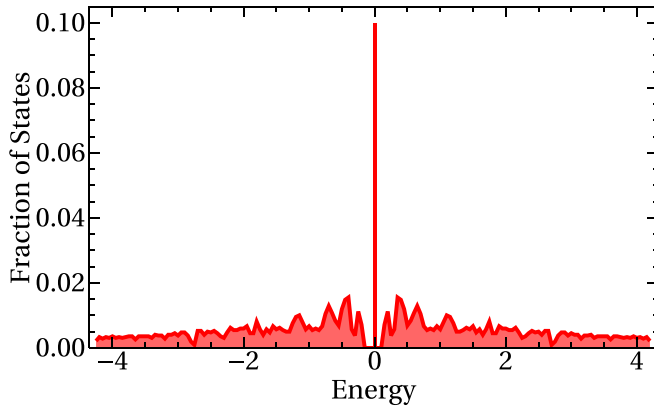


FIG. 5. The DOS of the rhombus lattice shown here is similar to the DOS of the kite-and-dart lattice in Fig. 3, however, the origin of the zero-energy peak is completely different.

isolated domains. Within each domain all the excluded sites are of the same color, i.e., they belong to the same (minority) sublattice. Note that in the smallest two domains there are a few accidental excluded sites on the majority sublattice; two are shown in the bottom-left corner in Fig. 7. While the zero-energy states coming from bipartite mismatch are required to have amplitude only on the majority sublattice, they are not required to have amplitude on all such sites. However, these accidental excluded sites are not robust in the way our main findings are. For instance, applying any magnetic field eliminates them and causes the zero-energy states to have amplitude on all majority sublattice sites. In the adjacent domain, all the excluded sites again belong to one (minority) sublattice only, which is, however, the opposite sublattice from the previous domain.

One may count the sublattice mismatch locally for each domain and add up their absolute values for the entire lattice, i.e., compute $\langle (-1)^{\mathcal{S}_r} \Delta n(\mathbf{r}) \rangle$, where \mathcal{S}_r is ± 1 for each domain. The result of that calculation is shown in Fig. 6 as the “local” mismatch. It is clear that for large lattice sizes the local

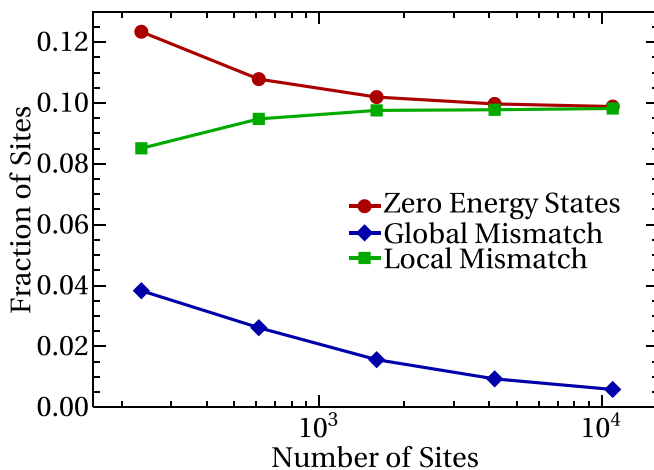


FIG. 6. Fractions for the mismatch in the number of sites in the two sublattices (global and local, as defined in the text) and for the number of zero-energy states as a function of the total number of sites in the rhombus lattice.

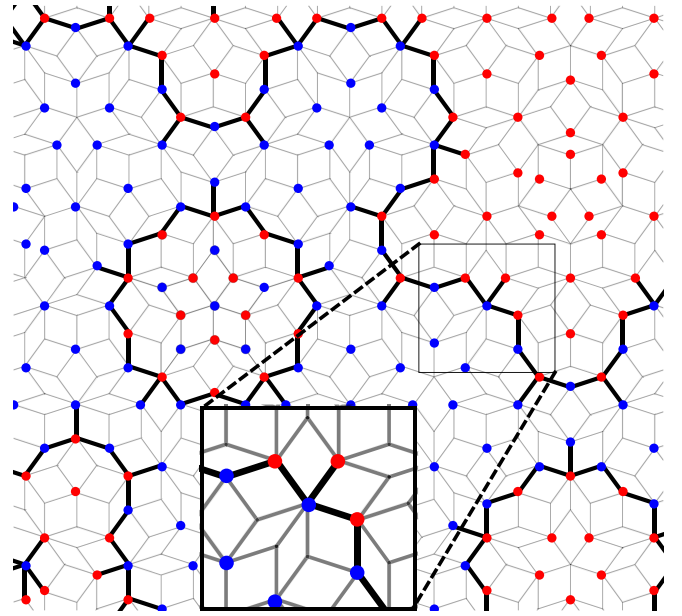


FIG. 7. Excluded sites for a portion of the rhombus lattice. They are shown in red or blue based on which of the two global sublattices they belong to. Bold links, connecting red and blue excluded sites, constitute the boundaries of the domains.

mismatch, defined this way, indeed asymptotically accounts for all zero-energy states, with differences at finite lattice size coming from our choice of open boundary conditions. The problem, however, is that the lattice is not cut across the bold links in Fig. 7 and therefore the domains are actually coupled. One thus might expect that the coupling lifts the macroscopic degeneracy of the zero-energy states.

To understand why the degeneracy is intact, consider a Hamiltonian for two neighboring domains, grouping sites by the domain, (1,2), and the sublattice within a domain (A, B), letting the A sublattice be the minority one for each domain. As we see later, this means that sublattices A_1 and A_2 are not on the same global sublattice. The corresponding Hamiltonian is

$$H' = \begin{matrix} & \begin{matrix} A_1 & B_1 & A_2 & B_2 \end{matrix} \\ \begin{matrix} A_1 \\ B_1 \\ A_2 \\ B_2 \end{matrix} & \begin{pmatrix} 0 & G_1 & C & 0 \\ G_1^T & 0 & 0 & 0 \\ C^T & 0 & 0 & G_2 \\ 0 & 0 & G_2^T & 0 \end{pmatrix} \end{matrix}. \quad (2)$$

Each domain, 1 and 2, is represented by a usual bipartite lattice Hamiltonian, Eq. (1). The two are coupled by the C term connecting solely the minority sites in domain 1 to the minority sites in the domain 2. This is because the bold links in Fig. 7 connect only the minority lattice sites in both domains. From this it is clear that if $\psi_0 = (0, \vec{x}_1)^T$ is a zero eigenstate of the first domain, considered in isolation, then there is a corresponding localized zero eigenstate of the whole system, $\Psi_0 = (0, \vec{x}_1, 0, 0)^T$. A similar analysis holds for the second domain. An equivalent way to see this is that, since the domains are only joined along the sites with no amplitude (excluded sites) for all zero-energy states, the coupling cannot

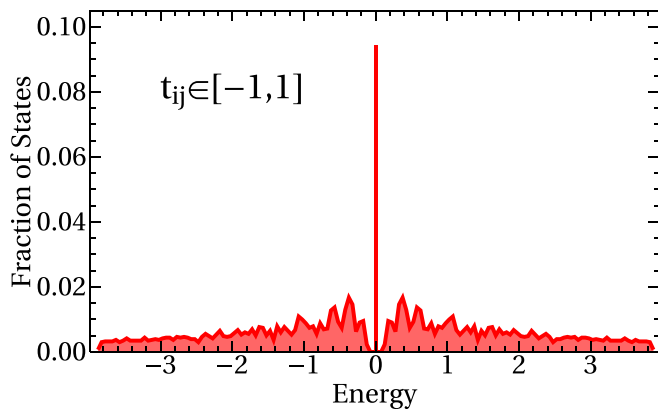


FIG. 8. DOS for a Penrose lattice with random nearest-neighbor hopping amplitudes drawn uniformly from $t_{ij} \in [-1, 1]$ (one realization).

perturb these states. This pattern also requires that the global sublattices, occupied with the excluded sites, switch between the adjacent domains.

Therefore, from the viewpoint of the zero-energy states, the quasicrystal is partitioned into strictly disconnected domains. One can thus choose a basis where all zero-energy states are confined to the majority lattice of one of the domains. As a result, counting the *local* sublattice mismatch (i.e., inside each domain), $\langle (-1)^{S_r} \Delta n(\mathbf{r}) \rangle$, gives an accurate count of the zero-energy states, as shown in Fig. 6. It is important to stress that the “domain walls” are impenetrable only for the zero-energy states. All other states (90%) are not localized to the domains and propagate freely between them.

Looking at the large-scale structure of the rhombus lattice one can find domains with sizes at all scales. Figure 1 shows a larger portion of the lattice divided into its domains. These have been colored red or blue based on which (global) sublattice the excluded sites occupy in that domain. There are domains contained in other, larger domains; looking at increasingly large portions of the lattice, these domains continue to arbitrarily large length scales. As one can see, these domains have the same self-similar structure as the Penrose lattice [14,30–33].

Therefore, a theory that explains the fraction of zero-energy states must be capable of explaining this self-similarity structure of the domain shapes and sizes. In Sec. IV, we will develop a real-space RG treatment of the Penrose lattice growth, based on its inflation property [41]. The number of inflation generations serves as the RG “time.” We find that this treatment is capable of accurately predicting the number of domains and their size distribution.

III. PERTURBATIONS OF THE ZERO-ENERGY STATES

A. Robustness to perturbations

The existence of the zero-energy states appears to be completely or partially robust against a number of perturbations of the initial model. Figure 8 shows the DOS of the Penrose lattice with random nearest-neighbor hopping, t , drawn from a box distribution, $t \in [-1, 1]$. The number of zero-energy states is the same as in the constant- t model. This is not

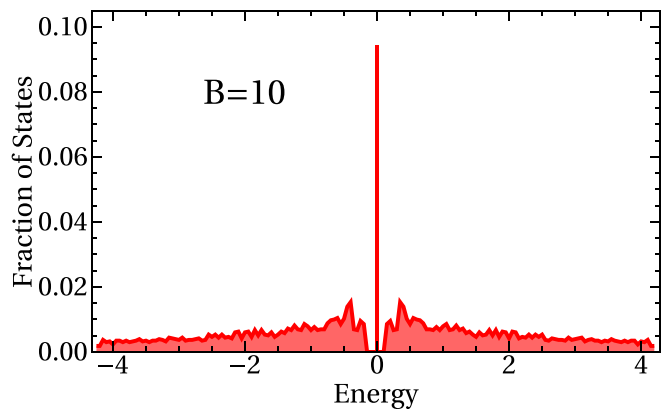


FIG. 9. DOS for a Penrose lattice in the presence of a perpendicular magnetic field of half-flux quanta per small rhombus.

surprising, since both the domain structure and the mismatch count rely only on the geometry of the lattice, and not on specific hopping amplitudes. The same reasoning explains why a perpendicular magnetic field does not change the number of zero-energy states (Fig. 9). Indeed, the magnetic field enters as complex phases of the hopping amplitudes. Note that both random hopping and the magnetic field do affect the DOS of nonzero-energy states.

Slightly less obvious is the effect of random dilution of the lattice by removal of random sites. We found that this leads to a slow suppression of the number of zero-energy states, but not to their immediate disappearance. This is also easy to understand, since the removal of the sites does not affect domain partitioning, but only removes sites from the interior or the boundary of a domain. Depending on whether a minority or a majority sublattice site is removed, the mismatch increases or decreases by one, adding or removing a zero-energy state to or from the domain. Since it is $\approx 10\%$ more likely to remove a majority site, there is a slight tendency towards a decreasing number of zero-energy states upon dilution.

The most severe perturbation is the addition of NNN (i.e., along diagonals of some rhombuses) hopping amplitudes. Such a perturbation violates the bipartite nature of the lattice. If introduced across the domain boundary, it leads to interdomain coupling involving the majority sublattices. This could potentially eliminate all zero-energy states in both domains. Yet this is not the case, as shown in Fig. 10, where we add NNN hopping in randomly chosen bonds. Each NNN link eliminates zero, one, or at most two zero-energy states, depending on how many local majority sublattice sites it connects. Within a given domain one may choose a basis in the null space, where all but one zero-energy state have no amplitude at a given site of the majority sublattice. Thus, if this site is involved in an NNN link, only the single state acquires a matrix element, which shifts it away from zero energy. As a result, if less than $\approx 20\%$ of sites participate in NNN links, a fraction of the zero-energy states persists.

B. Spatial structure of the zero-energy states

Since all zero-energy states are exactly degenerate, one can choose any orthogonalized linear combination as a basis. One can always choose it to respect the domain structure,

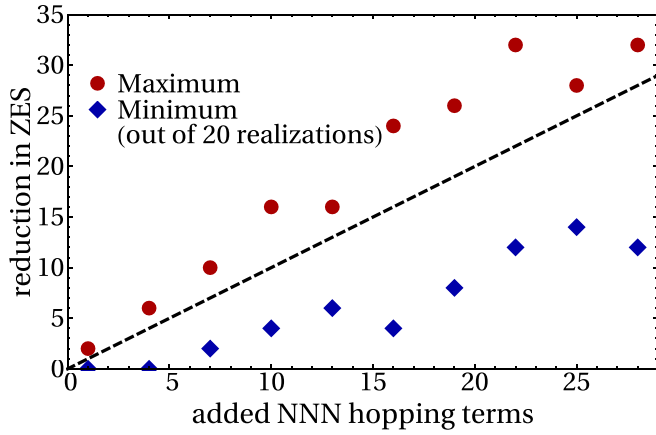


FIG. 10. Number of zero-energy states (ZES) removed upon the addition of random NNN links. A site was randomly chosen, and a hopping amplitude was added to a random NNN of this site. Twenty realizations were considered; here, we plot only the maximal and minimal reductions of zero-energy states. The dashed line has slope 1 and is just a guide for the eyes. The lattice contains 4581 sites and 441 zero-energy states.

i.e., each state in the basis is fully localized within (the majority sublattice of) one domain and has zero overlap with states from all other domains. It is less straightforward to characterize individual states within a domain. To this end it is convenient to define the *basis-independent* projection matrix as

$$P_{ij} = \sum_{\alpha} \langle i | \Psi^{(\alpha)} \rangle \langle \Psi^{(\alpha)} | j \rangle, \quad (3)$$

where α labels zero-energy states, i and j label lattice sites, and $\Psi^{(\alpha)}$ is the wave function corresponding to the α zero-energy state. The projection matrix, P_{ij} , has block-diagonal form in the space of the domains, with nonzero elements only on the majority sublattice of the corresponding domain.

Consider now a small local (i.e., at site k) perturbation of the on-site energy $V_{ij} = V \delta_{ik} \delta_{jk}$. In first-order degenerate perturbation theory, the energies of the zero-energy states are shifted by the eigenvalues of the matrix

$$V^{\alpha\beta} = \langle \Psi^{(\alpha)} | V | \Psi^{(\beta)} \rangle = V \langle \Psi^{(\alpha)} | k \rangle \langle k | \Psi^{(\beta)} \rangle. \quad (4)$$

This is a rank 1 matrix with all eigenvalues, except one, equal to 0. Its only nonzero eigenvalue, δE , and the corresponding eigenfunction, $\Phi_i^{(k)}$, are given by

$$\delta E = V P_{kk}, \quad \Phi_i^{(k)} = P_{ik} / \sqrt{P_{kk}}. \quad (5)$$

This means that the local perturbation (if on the majority sublattice) shifts the energy of a *single* zero-energy state. Both the energy shift and the corresponding eigenfunction $\Phi_i^{(k)}$, localized around site k , are given in terms of the k th column of the projection matrix P_{ik} . Note that $\sum_k P_{kk} =$ the number of zero-energy states. As a result, the average energy shift susceptibility is $\delta E / V = 2f / (1 + f) \approx 0.179$, where $f = 0.098$ is the fraction of zero-energy states and the averaging is performed over the majority sublattice.

Figure 11 shows the distribution of the diagonal elements of the projection matrix, P_{ii} , for the lattice with 4581 sites,

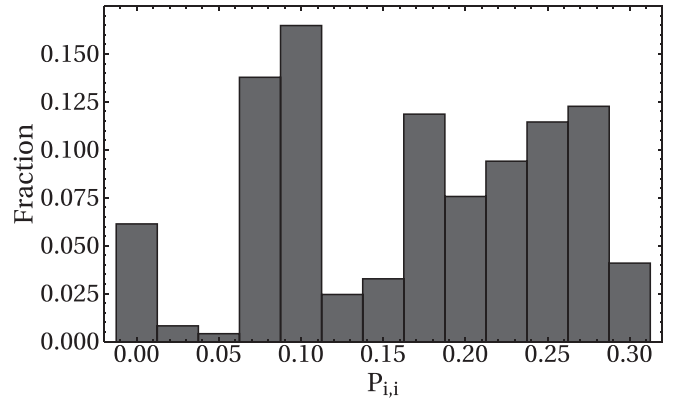


FIG. 11. Histogram of the diagonal entries of the projection matrix, P_{ij} , which determines the perturbative energy shift due to a local on-site potential (only the majority sublattice is kept).

colored in Fig. 1, which contains 441 zero-energy states. As expected, the mean susceptibility is about 0.18, while the standard deviation is 0.085. Figure 12 shows log-plots of $P_{ik} \propto \Phi_i^{(k)}$ as a function of the distance $|\mathbf{r}_i - \mathbf{r}_k|$ in units of the rhombus side. Four randomly chosen sites k are shown, while *all* other sites exhibit the same pattern. It is evident that $\Phi_i^{(k)} \approx \sqrt{P_{kk}} \exp[-|\mathbf{r}_i - \mathbf{r}_k| / \xi_k]$, where the localization length $\xi_k = 2.4 \pm 0.2$. We thus conclude that local perturbations of the zero-energy manifold lead to a spatially localized response within the given domain.

IV. REAL-SPACE RENORMALIZATION GROUP

A. Background

We now develop a method to find the local sublattice mismatch and the number of domains in lattices of progressively increasing sizes. There are only eight distinct site types in the Penrose rhombus lattice. We follow the standard notations given in, e.g., Ref. [42], which are specified in Fig. 13. Therefore a finite patch of the lattice can be characterized by

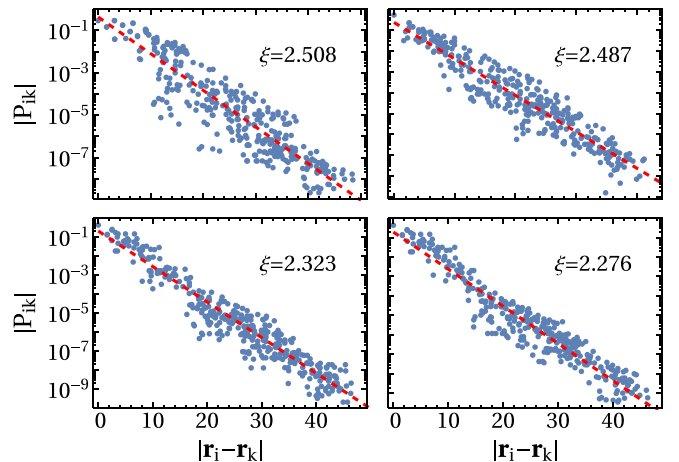


FIG. 12. Wave functions of the perturbed states for perturbations at four sites. The horizontal axis is the distance from the perturbation site in units of the rhombus edge length. The best-fit localization lengths, ξ_k , are shown.

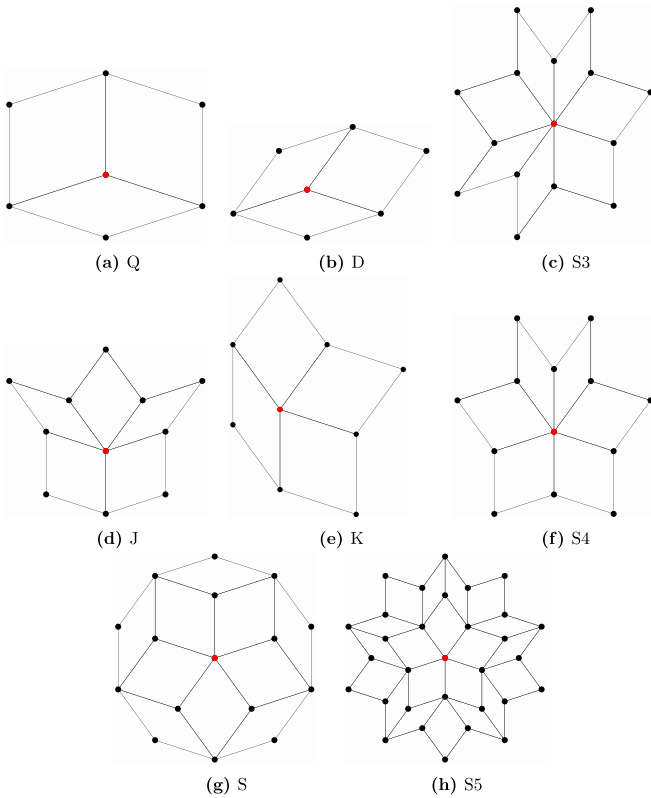


FIG. 13. The neighborhoods associated with each of the eight distinct types of sites. Each neighborhood uniquely identifies the central red site.

an eight-dimensional vector, \vec{n} , whose entries correspond to the number of sites of a given type:

$$\vec{n} = (Q \ D \ S3 \ J \ K \ S4 \ S \ S5)^T. \quad (6)$$

The key to our approach is the *inflation property* of the Penrose lattice [41]. This is a set of partition rules for all rhombuses that, when followed by a linear rescaling by τ , generates another valid patch of the lattice with more sites. Since the rules are local and specific to a given type of the vertex, they can be represented as a matrix acting on the vector \vec{n} . In the bulk, this matrix is given by

$$M = \begin{pmatrix} 0 & 2 & 3 & 1 & 1 & 4 & 5 & 0 \\ 1 & 0 & 0 & 0 & 0 & 0 & 0 & 0 \\ 0 & 1 & 0 & 0 & 0 & 0 & 0 & 0 \\ \frac{2}{3} & \frac{1}{3} & 0 & \frac{2}{3} & 1 & 0 & 0 & \frac{5}{3} \\ 0 & 0 & 0 & 1 & 0 & 0 & 0 & 0 \\ 0 & 0 & 0 & 0 & 1 & 0 & 0 & 0 \\ 0 & 0 & 0 & 0 & 0 & 0 & 0 & 1 \\ 0 & 0 & 1 & 0 & 0 & 1 & 1 & 0 \end{pmatrix}. \quad (7)$$

The fractional numbers reflect the fact that a given site may be shared by several adjacent neighborhoods. This sharing is modified at the boundaries of the lattice. Thus the boundaries require some care and are dealt with in Appendix B. For now we proceed with the bulk of the lattice.

Given the matrix M , one can compute the site counts after k inflations with some initial state \vec{n}_1 ,

$$\vec{n}_k = M^k \vec{n}_1. \quad (8)$$

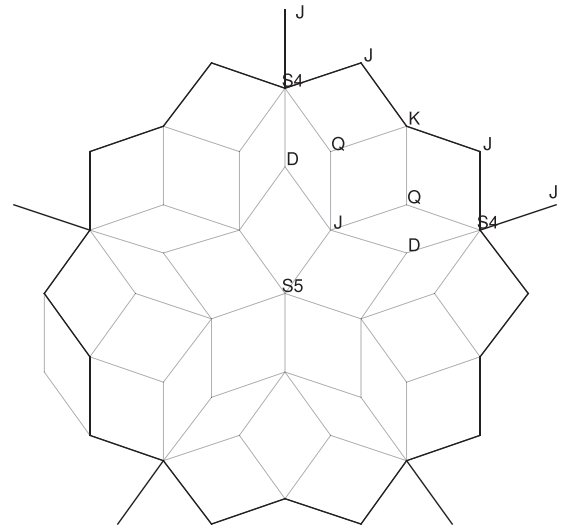


FIG. 14. A new emergent domain, obtained after two inflations of the S5 neighborhood. Sites are labeled according to the convention in Fig. 13. All other domains are results of the repeated inflations of this patch. It is also used as the initial seed to generate Penrose rhombus lattices with a larger number of sites via the inflation process.

The asymptotic growth rate of the number of sites as a function of the generation number is given by the matrix's largest eigenvalue τ^2 , where τ is the golden ratio. We can also find the relative distribution of site types in the infinite lattice as the corresponding eigenvector,

$$\left(\frac{1}{\tau^2} \quad \frac{1}{\tau^4} \quad \frac{1}{\tau^6} \quad \frac{1}{\tau^3} \quad \frac{1}{\tau^5} \quad \frac{1}{\tau^7} \quad \frac{1}{\tau^6(1+\tau^2)} \quad \frac{1}{\tau^4(1+\tau^2)} \right), \quad (9)$$

which reproduces the known distribution, see Ref. [43].

Looking at Fig. 1, there are a number of domains of different shapes and sizes. In fact, all are generated from repeated inflations of a single “seed” domain. For example, the seed domain may be chosen as depicted in Fig. 14. Upon repeated inflation steps it generates self-contained domains, all bounded by a line of excluded sites. Choosing this starting configuration also simplifies properly accounting for the boundary, the details of which are dealt with in Appendix B.

Computing the local mismatch requires two inputs. The first is the number of new domains generated at the k th inflation step, A_k . These newly born domains with the shape of the initial seed (Fig. 14) may be seen in Figs. 1 and 7. Inspection shows that *all* new domains originate from the S5 neighborhoods (see Fig. 13) after two inflation iterations. We thus find

$$A_k = (\vec{n}_{k-2})_{S5}. \quad (10)$$

The second input is the global mismatch, G_k , of A and B sublattices after k generations. To find it, one needs to double the counting vector \vec{n} to keep track of which sublattice a given site belongs to: $\vec{n} = (\vec{n}_A, \vec{n}_B)^T$. Correspondingly, the M matrix also becomes 16×16 and is presented in Appendix A. The

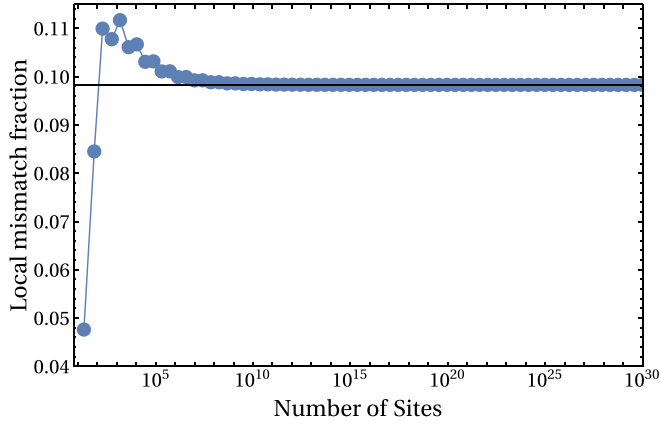


FIG. 15. Local mismatch fraction, L_k/N_k , as a function of the total number of sites after k inflations, $N_k = \sum_i (\bar{n}_k)_i$.

global mismatch is given by

$$G_k = \sum_{i \in A} (\bar{n}_k)_i - \sum_{i \in B} (\bar{n}_k)_i, \quad (11)$$

which may be either positive or negative.

With these two inputs, one can now evaluate the sum of all domain-specific local mismatches, L_k , after k inflation steps. This is equivalent to the “order parameter” $\langle (-1)^{S_\tau} \Delta n(\mathbf{r}) \rangle$ introduced above and, as explained, is exactly the number of zero-energy states in the DOS of the rhombus lattice. In Appendix D, we show that it is given by

$$L_k = G_k + 2 \sum_{l=1}^{k-1} A_{k-l} G_l. \quad (12)$$

Equations (7)–(12) provide a complete iterative scheme to evaluate the number of zero-energy states starting from any seed. It is straightforward to iterate them to calculate the local mismatch for extremely large systems. Figure 15 shows the result of such iteration for up to 70 generations with $\sim 10^{30}$ sites. After some initial fluctuations the mismatch as a fraction of total sites converges to $81 - 50\tau \approx 0.0983$.

We now proceed to derive this result analytically. The largest (nondegenerate) eigenvalue of the M matrix is τ^2 , signaling that the total number of sites, N_k , and the number of new domains, A_k , both scale as τ^{2k} . Thus, for $k \gg 1$, with exponential accuracy,

$$\begin{aligned} N_k &= \langle \bar{\mathbb{1}} | \psi_1 \rangle \tau^{2k} \langle \psi_1 | \bar{n}_1 \rangle, \\ A_k &= \langle \bar{S}5 | \psi_1 \rangle \tau^{2(k-2)} \langle \psi_1 | \bar{n}_1 \rangle, \end{aligned} \quad (13)$$

where $|\psi_1\rangle$ is the eigenvector corresponding to the largest eigenvalue, $\langle \bar{\mathbb{1}} |$ is the vector whose entries consist of 1, and $\langle \bar{S}5 |$ is a projection onto the $S5$ component. On the other hand, the global mismatch is given by $G_k = \langle \{\bar{\mathbb{1}}, -\bar{\mathbb{1}}\} | M^k | \bar{n}_1 \rangle$, where $\langle \{\bar{\mathbb{1}}, -\bar{\mathbb{1}}\} |$ has 1 on entries corresponding to one sublattice and -1 on the other sublattice. It scales only as the second-largest eigenvalue, since $\langle \{\bar{\mathbb{1}}, -\bar{\mathbb{1}}\} | \psi_1 \rangle = 0$. The second-largest eigenvalue is 2 (note that the boundary has to be included to arrive at this number) and thus $G_k \propto 2^k$. Therefore, as already mentioned, $G_k \ll N_k, A_k, L_k$ for $k \gg 1$. Moreover, Eq. (12)

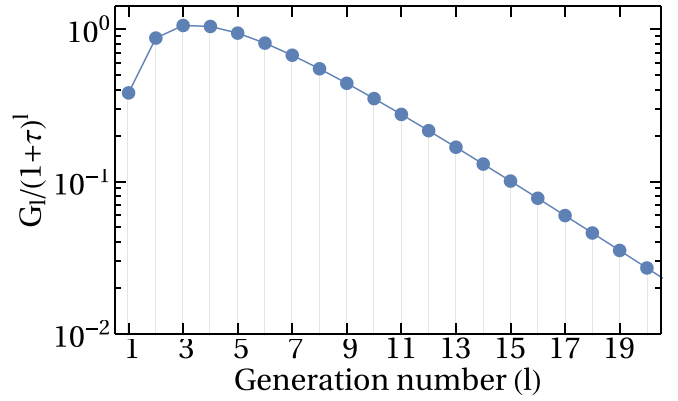


FIG. 16. Plot of G_l/τ^{2l} , the summand in Eq. (15), which is proportional to the relative contribution of a domain of size/age l to the number of zero-energy states.

simplifies to

$$\begin{aligned} L_k &\approx 2 \sum_{l=1}^{k-1} A_{k-l} G_l = 2 \langle \bar{S}5 | \psi_1 \rangle \langle \psi_1 | \bar{n}_1 \rangle \sum_{l=1}^{k-1} \tau^{2(k-l-2)} G_l \\ &= \frac{2 \langle \bar{S}5 | \psi_1 \rangle \langle \psi_1 | \bar{n}_1 \rangle}{\tau^4} \tau^{2k} G(\tau^{-2}), \end{aligned} \quad (14)$$

where

$$G(\tau^{-2}) = \sum_{l=1}^{\infty} \frac{G_l}{\tau^{2l}} \equiv G, \quad (15)$$

and we have extended the sum to infinity, since it is exponentially convergent. The fraction of zero-energy states is thus

$$\frac{L_k}{N_k} = \frac{\langle \bar{S}5 | \psi_1 \rangle}{\langle \bar{\mathbb{1}} | \psi_1 \rangle} \frac{2G}{\tau^4}. \quad (16)$$

The ratio $\langle \bar{S}5 | \psi_1 \rangle / \langle \bar{\mathbb{1}} | \psi_1 \rangle = 1/\tau^4(1 + \tau^2) \approx 0.04$ is the global fraction of $S5$ sites, given by the last entry in Eq. (9). We thus obtain

$$\frac{L_k}{N_k} = \frac{2G}{\tau^4(1 + \tau^2)\tau^4} = 81 - 50\tau, \quad (17)$$

where we have used that $2G = 7 + 6\tau$, as evaluated in Appendix C.

While this value agrees with previous reports [29–31], our approach provides interesting additional information. Figure 16 shows $\ln[\tau^{-2l} G_l]$ as a function of the generation “age” l . According to Eq. (15), this quantity measures the relative contributions to the number of zero-energy states of domains of “age” l , i.e., size N_l . The latter tells over how many lattice sites the corresponding zero-energy states are extended. One notes that about half of the zero states are localized within “young” compact domains with $l \leq 5$. The remaining half falls within an exponential tail of larger “older” domains. For those we find a *scaling law* for relative number of zero-energy states, $Z(N)$, extended over $N > N_5$ lattice sites:

$$Z(N) \propto N^{-\eta}, \quad \eta = 1 - \frac{\ln 2}{2 \ln \tau} \approx 0.2798. \quad (18)$$

Indeed, since τ^2 and 2 are the largest and the second-largest eigenvalues of the M matrix, for $l \gtrsim 6$, one finds $\ln Z =$

$\ln[\tau^{-2l}G_l] \approx -l \ln[\tau^2/2]$. On the other hand, $\ln N = l \ln \tau^2$, from which Eq. (18) follows.

V. CONCLUSIONS

We have discussed the nature of the zero-energy states in Penrose quasicrystals. We have shown that the lattice is subdivided into a nested structure of self-similar domains. Upon inflation, the domains are inevitably born from every $S5$ -neighborhood site and continue to grow indefinitely, while new domains appear inside older ones. The domain boundaries have a property of being impenetrable walls for the zero-energy states (but not for any other states). As a result, each domain contributes a number to the total of zero-energy states given by the mismatch between A and B sublattices within this domain. The mismatches alternate between successive domains, yielding no global mismatch. Yet, $\sim 10\%$ of all states are at exactly zero energy, due to the combined local mismatches in all the domains. The macroscopically degenerate zero-energy states may be chosen to be localized within the respective domains.

Utilizing the self-similar structure of the domains, we developed a real-space RG evolution procedure, where the generation number, k , plays the same role as the RG “time.” Note that the lattice size N_k grows exponentially with “time” as $N_k \sim \tau^{2k}$. In other words, $k \sim \ln N_k$, as is common for the real-space RG. This procedure is capable of accurately counting domains, their sizes, and the sublattice mismatch. It reproduces the $81 - 50\tau \approx 0.0983$ fraction of the zero-energy states, derived before from different perspectives [29–31].

The zero-energy states and the domains supporting them are robust against a number of perturbations. Random hopping and magnetic field do not alter their number at all. Random dilution of the lattice leads to a very slow decrease in their number. Finally, the inclusion of NNN links, which violate the bipartite property of the original lattice, kills them at the average rate of a single state per NNN link.

The robustness of the domain structure and the zero-energy states inside the domains raises the question whether they are of a topological origin, connecting to previous work on topological states in this system [44–46]. We have not been able to find convincing arguments for or against this premise. One tantalizing observation is that the Penrose lattice is a cross section of a five-dimensional cubic crystal. The latter has a bipartite structure, which is directly inherited by the Penrose tiling. The bipartite hopping Hamiltonian belongs to the BD1 Altland-Zirnbauer symmetry class [47], which is topological in five dimensions with the Z homotopy group. One may thus wonder whether the domains and zero-energy states may be a legacy of their 5D topological parent.

ACKNOWLEDGMENTS

We thank F. Burnell and H. Manoharan for fruitful discussions. E.D.-R. and R.M.F. were supported by the National Science Foundation through the UMN MRSEC under Grant No. DMR-1420013. A.K. was supported by NSF Grant No. DMR-1608238.

APPENDIX A: INFLATION PROCEDURE WITH SUBLATTICES

To calculate the global mismatch we need to track the sublattice that each site belongs to. We double the length of the \vec{n} vector that counts sites, now tracking A sites and B sites separately:

$$\vec{n} = (\vec{n}_A \quad \vec{n}_B)^T \\ = (Q_A \quad D_A \quad S3_A \quad \dots \quad Q_B \quad D_B \quad S3_B \quad \dots).$$

Now we can write the inflation matrix in block form, in terms of whether the new sites are on the same sublattice (AA subscript) or opposite sublattices (AB subscript) as the original site:

$$M' = \begin{pmatrix} M_{AA} & M_{AB} \\ M_{AB} & M_{AA} \end{pmatrix}. \quad (\text{A1})$$

That the diagonal blocks and off-diagonal blocks are the same comes from our freedom to choose which sublattice we label A . To keep the total number of sites the same as in the original matrix we must have $M_{AA} + M_{AB} = M$. So it is sufficient to give only one block explicitly:

$$M_{AA} = \begin{pmatrix} 0 & 2 & 0 & 0 & 1 & 0 & 0 & 0 \\ 1 & 0 & 0 & 0 & 0 & 0 & 0 & 0 \\ 0 & 0 & 0 & 0 & 0 & 0 & 0 & 0 \\ 0 & \frac{1}{3} & 0 & 0 & 1 & 0 & 0 & \frac{5}{3} \\ 0 & 0 & 0 & 1 & 0 & 0 & 0 & 0 \\ 0 & 0 & 0 & 0 & 0 & 0 & 0 & 0 \\ 0 & 0 & 0 & 0 & 0 & 0 & 0 & 0 \\ 0 & 0 & 1 & 0 & 0 & 1 & 1 & 0 \end{pmatrix}. \quad (\text{A2})$$

APPENDIX B: BOUNDARY CONTRIBUTIONS

To account for boundary contributions, we separately track the number of sites on the boundary and in the bulk. Then we can use different rules to evolve the boundary and add boundary effects on interior sites near the boundary. For the starting geometry considered here, the boundary is composed of only four kinds of sites: J , K , $S4$, and $S3$. We can add the counts of these sites by appending them to the end of our vector \vec{n} , leaving it with 12 entries:

$$\vec{n}_1 = (\underbrace{10 \ 5 \ 0 \ 5 \ 0 \ 0 \ 1 \ 0}_{\text{previous vector}} \ \underbrace{15 \ 5 \ 5 \ 0}_{\text{boundary entries}}). \quad (\text{B1})$$

The transition matrix will have the general structure

$$M_1 = \begin{pmatrix} M & B' \\ 0 & B \end{pmatrix}. \quad (\text{B2})$$

Here M is the same bulk matrix as above, B is the matrix describing the evolution of the boundary, and B' gives the contribution of the boundary sites to the bulk counts. We note that the details of B and B' depend on the geometry. Here the boundary is not exactly the geometrical boundary but, rather, is defined by the rings of excluded sites.

The main complication from adding the boundary is that the B' matrix is not the same across inflations. Specifically, it alternates between two versions. This is reflected in the structure of the boundary, since it alternates between two sites bordering the interior, $S3$ and J (see Fig. 17). The type of inward-facing site changes the boundary effect on the interior.

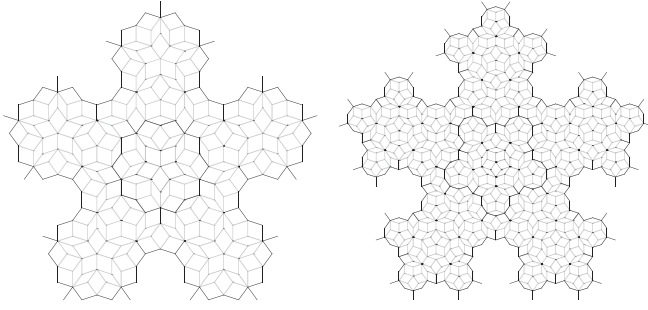


FIG. 17. Boundaries for successive inflations. Note the $S3$ sites and J sites on the inward-facing boundary on the left and right, respectively.

The matrices are explicitly given by

$$B = \begin{pmatrix} 1 & 1 & 1 & 1 \\ 1 & 0 & 0 & 0 \\ 0 & 1 & 0 & 0 \\ 1 & -1 & 0 & 0 \end{pmatrix}, \quad (\text{B3})$$

$$B'_{\text{even}} = \begin{pmatrix} 1 & 1 & 0 & 0 \\ 0 & 0 & 0 & 0 \\ 0 & 0 & -2 & 0 \\ 0 & 0 & -\frac{2}{3} & 0 \\ 0 & 0 & 0 & 0 \\ 0 & 0 & 0 & 0 \\ 0 & 0 & 0 & 0 \\ 0 & 0 & 0 & 0 \end{pmatrix}, \quad B'_{\text{odd}} = \begin{pmatrix} 0 & 0 & 4 & 3 \\ 0 & 0 & 0 & 0 \\ 0 & 0 & 0 & 0 \\ 0 & -\frac{4}{3} & 0 & 0 \\ 0 & 0 & 0 & 0 \\ 0 & 0 & 0 & 0 \\ 0 & 0 & 0 & 0 \\ 0 & 0 & 1 & 1 \end{pmatrix}. \quad (\text{B4})$$

The negative entries come from sites moving between the boundary and the bulk. In B'_{even} and B'_{odd} , they come from sites being included on the inward-facing “spikes” of the boundary.

These can also be extended to track the sublattice to which the sites belong, as in Appendix A. All matrices have the structure of Eq. (A1) and obey the same constraint $M_{AA} + M_{AB} = M$, so we just give the AA components, as in Eq. (A2):

$$B_{AA} = \begin{pmatrix} 0 & 1 & 1 & 1 \\ 1 & 0 & 0 & 0 \\ 0 & 0 & 0 & 0 \\ 1 & 0 & 0 & 0 \end{pmatrix}, \quad (\text{B5})$$

$$B'_{\text{even},AA} = \begin{pmatrix} 0 & \frac{2}{3} & 0 & 0 \\ 0 & 0 & 0 & 0 \\ 0 & 0 & 0 & 0 \\ 0 & 0 & -\frac{2}{3} & 0 \\ 0 & 0 & 0 & 0 \\ 0 & 0 & 0 & 0 \\ 0 & 0 & 0 & 0 \\ 0 & 0 & 0 & 0 \end{pmatrix},$$

$$B'_{\text{odd},AA} = \begin{pmatrix} 0 & 0 & 0 & 0 \\ 0 & 0 & 0 & 0 \\ 0 & 0 & 0 & 0 \\ 0 & -\frac{4}{3} & 0 & 0 \\ 0 & 0 & 0 & 0 \\ 0 & 0 & 0 & 0 \\ 0 & 0 & 0 & 0 \\ 0 & 0 & 1 & 1 \end{pmatrix}. \quad (\text{B6})$$

TABLE II. Parameters for the calculation of G .

i	w_i	λ_i	$\langle \{\vec{1}, -\vec{1}\} i \rangle$	$\langle \{\vec{1}, -\vec{1}\} M_{\text{odd}} i \rangle$
2	$\frac{10}{3}$	4	$\frac{18}{5}$	$\frac{36}{5}$
4	$-\frac{\tau}{2}$	τ^2	$4 + 6\tau$	$6 + 10\tau$
13	$-\frac{1}{2} + \frac{\tau}{2}$	$2 - \tau$	$10 - 6\tau$	$16 - 10\tau$

APPENDIX C: CALCULATION OF G

As just discussed, when accounting for the boundary, inflation behaves differently for even and odd generations. Thus, we must treat even and odd terms separately. Starting from our initial vector $|\vec{n}_1\rangle$, Eq. (8), for an even number of inflations we can write

$$|\vec{n}_{2k+1}\rangle = (M_{\text{even}}M_{\text{odd}})^k |\vec{n}_1\rangle. \quad (\text{C1})$$

We can expand in eigenvectors and eigenvalues, $\{|i\rangle\}$, λ_i , of $(M_{\text{even}}M_{\text{odd}})$,

$$|\vec{n}_{2k+1}\rangle = \sum_i \lambda_i^k w_i |i\rangle, \quad (\text{C2})$$

where w_i are the weights connecting $|\vec{n}_1\rangle$ to $|i\rangle$. These are not $\langle i | \vec{n}_1 \rangle$ because $(M_{\text{even}}M_{\text{odd}})$ is not symmetric and hence the $|i\rangle$ are not orthogonal. But nevertheless, the weights exist and are unique.

The mismatch after an even number of inflations is

$$G_{2k+1} = \langle \{\vec{1}, -\vec{1}\} | \vec{n}_{2k+1} \rangle = \sum_i \lambda_i^k w_i \langle \{\vec{1}, -\vec{1}\} | i \rangle. \quad (\text{C3})$$

From the product of the weights and the inner product, only three terms are nonzero, as listed in Table II.

For odd numbers of inflations we can define a similar expansion:

$$G_{2k+2} = \langle \{\vec{1}, -\vec{1}\} | \vec{n}_{2k+2} \rangle = \sum_i \lambda_i^k w_i \langle \{\vec{1}, -\vec{1}\} | M_{\text{odd}} | i \rangle. \quad (\text{C4})$$

Plugging in the summation for G , Eq. (15), we obtain

$$\sum_{k=1}^{\infty} \frac{G_k}{\tau^{2k}} = \sum_{k=0}^{\infty} \frac{G_{2k+1}}{\tau^{4k+2}} + \sum_{k=0}^{\infty} \frac{G_{2k+2}}{\tau^{4k+4}} \quad (\text{C5})$$

$$= \left(\frac{75}{44} + \frac{63}{44}\tau \right) + \left(\frac{91}{44} + \frac{57}{44}\tau \right) \quad (\text{C6})$$

$$= \frac{7}{2} + 3\tau \approx 8.3541. \quad (\text{C7})$$

APPENDIX D: DERIVATION OF THE EQUATION FOR L_k

To derive Eq. (12), we start by noting that the smaller domains in Fig. 1 look like the full lattice at an earlier stage of its evolution. We define the *exterior* region as the single domain that borders the boundary of the lattice. In Fig. 1 this is the large blue region. Next we define the *top-level* domains as domains that border this exterior region and hence are not contained inside anything except the exterior region. All red domains in Fig. 1 are top level, while only the small blue domain contained inside the central red domain is not top level. The number of *new* top-level domains created within

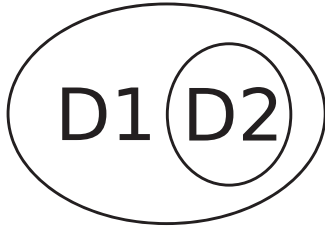


FIG. 18. Domain D1 contains another domain, D2.

the exterior (outer blue region in Fig. 1) in the k th generation is denoted T_k . We only count new top-level domains because we can trivially find the number of older top-level domains from this. A top-level domain never stops being top level, so the number of top-level domains of age l at a step k is merely the number of domains that were newly created exactly l generations ago, T_{k-l} .

Recall that the total number of new domains created at step k is A_k . Since domains of a given age are identical, we know that a domain of age l creates A_l new domains inside of it. As just mentioned, the number of top-level domains of age l at step k is T_{k-l} . Thus the number of new domains created inside domains of age l is $A_l T_{k-l}$. We can sum this over l to count all non-top-level domains created and subtract it from the total to find T_k ,

$$T_k = A_k - \sum_{l=1}^{k-1} A_l T_{k-l}. \quad (\text{D1})$$

Finally, we combine these relationships to find the total local mismatch, L_k , after k generations. We can use a summation similar to Eq. (D1) to recursively count the local mismatches from enclosed domains. At generation k there are T_{k-l} top-level domains of age l and each contributes L_l to the local mismatch. All that is left is then to count the mismatch of the exterior region (outer blue area in Fig. 1). We start with a simple example.

Consider a domain D1 with a single domain D2 inside of it, as shown in Fig. 18. Let the combined domain have a

mismatch ΔN (i.e., greater number of A sites than B sites) and the interior domain D2 have a mismatch $-\Delta N_{D2}$ (i.e., a greater number of B sites than A sites). It is negative because the majority sublattice switches when moving across the domain boundary. Then we have $\Delta N = \Delta N_{D1} - \Delta N_{D2}$, or $\Delta N_{D1} = \Delta N + \Delta N_{D2}$. Moreover, we have T_{k-l} domains of age l , each of which has a mismatch of G_l . Summing these contributions gives the mismatch in the exterior domain, $G_k + \sum_{l=1}^{k-1} G_l T_{k-l}$. Combining this with the local mismatches from the enclosed domains, we obtain an equation for the total local mismatch of the lattice after k inflations,

$$L_k = G_k + \sum_{l=1}^{k-1} G_l T_{k-l} + \sum_{l=1}^{k-1} L_l T_{k-l}. \quad (\text{D2})$$

Note that both equations, (D1) and (D2), are crucially based on the self-similarity property: domains of age l are identical to the entire lattice at the l th generation.

The next goal is to eliminate T_k from Eqs. (D1) and (D2). To this end, we encode the discrete sequences into generating functions, e.g.,

$$L(x) = \sum_{k=1}^{\infty} L_k x^k.$$

Since L_k increases exponentially as $\sim \tau^{2k}$, the series has a finite radius of convergence, $|x| < \tau^{-2}$. This allows us to rewrite the summations as algebraic multiplications:

$$A(x)T(x) = \sum_k \left[\sum_{l=1}^{k-1} A_l T_{k-l} \right] x^k.$$

Equations (D1) and (D2) then become algebraic, $T = A - AT$ and $L = G + GT + LT$, where we have omitted the argument x for brevity. From the first, one finds $T = A/(1 + A)$, and the second yields $L = G(1 + T)/(1 - T) = G(1 + 2A)$. Matching powers of x on either side of the equation gives Eq. (12).

-
- [1] D. Shechtman, I. Blech, D. Gratias, and J. W. Cahn, *Phys. Rev. Lett.* **53**, 1951 (1984).
- [2] T. Ishimasa, H.-U. Nissen, and Y. Fukano, *Phys. Rev. Lett.* **55**, 511 (1985).
- [3] N. Wang, H. Chen, and K. H. Kuo, *Phys. Rev. Lett.* **59**, 1010 (1987).
- [4] L. Bendersky, *Phys. Rev. Lett.* **55**, 1461 (1985).
- [5] L. Bindi, P. J. Steinhardt, N. Yao, and P. J. Lu, *Science* **324**, 1306 (2009).
- [6] Y. E. Kraus, Y. Lahini, Z. Ringel, M. Verbin, and O. Zeitler, *Phys. Rev. Lett.* **109**, 106402 (2012).
- [7] D. J. Apigo, W. Cheng, K. F. Dobiszewski, E. Prodan, and C. Prodan, *Phys. Rev. Lett.* **122**, 095501 (2019).
- [8] J. Zhao, S. Huo, H. Huang, and J. Chen, *Phys. Status Solidi Rapid Res. Lett.* **12**, 1800322 (2018).
- [9] A. Dureau, E. Levy, M. B. Aguilera, R. Bouganne, E. Akkermans, F. Gerbier, and J. Beugnon, *Phys. Rev. Lett.* **119**, 215304 (2017).
- [10] T. Watanuki, S. Kashimoto, D. Kawana, T. Yamazaki, A. Machida, Y. Tanaka, and T. J. Sato, *Phys. Rev. B* **86**, 094201 (2012).
- [11] M. Matsunami, M. Oura, K. Tamasaku, T. Ishikawa, S. Ideta, K. Tanaka, T. Takeuchi, T. Yamada, A. P. Tsai, K. Imura, K. Deguchi, N. K. Sato, and T. Ishimasa, *Phys. Rev. B* **96**, 241102(R) (2017).
- [12] E. C. Andrade, A. Jagannathan, E. Miranda, M. Vojta, and V. Dobrosavljević, *Phys. Rev. Lett.* **115**, 036403 (2015).
- [13] S. Matsukawa, K. Deguchi, K. Imura, T. Ishimasa, and N. K. Sato, *J. Phys. Soc. Jpn.* **85**, 063706 (2016).
- [14] S. Sakai, N. Takemori, A. Koga, and R. Arita, *Phys. Rev. B* **95**, 024509 (2017).
- [15] R. N. Araújo and E. C. Andrade, *Phys. Rev. B* **100**, 014510 (2019).
- [16] Y. Zhang, Y.-B. Liu, W.-Q. Chen, and F. Yang, *arXiv:2002.06485*.

- [17] Y. Cao, Y. Zhang, Y.-B. Liu, C.-C. Liu, W.-Q. Chen, and F. Yang, *Phys. Rev. Lett.* **125**, 017002 (2020).
- [18] K. Deguchi, S. Matsukawa, N. K. Sato, T. Hattori, K. Ishida, H. Takakura, and T. Ishimasa, *Nat. Mater.* **11**, 1013 EP (2012).
- [19] N. Hartman, W.-T. Chiu, and R. T. Scalettar, *Phys. Rev. B* **93**, 235143 (2016).
- [20] L. C. Collins, T. G. Witte, R. Silverman, D. B. Green, and K. K. Gomes, *Nat. Commun.* **8**, 15961 (2017).
- [21] D. Lenz, *Commun. Math. Phys.* **227**, 119 (2002).
- [22] D. Damanik and D. Lenz, *Commun. Math. Phys.* **207**, 687 (1999).
- [23] S. E.-D. Mandel and R. Lifshitz, *Philos. Mag.* **88**, 2261 (2008).
- [24] C. Sire, *Europhys. Lett.* **10**, 483 (1989).
- [25] T. Fujiwara and T. Yokokawa, *Phys. Rev. Lett.* **66**, 333 (1991).
- [26] X.-P. Tang, E. A. Hill, S. K. Wonnell, S. J. Poon, and Y. Wu, *Phys. Rev. Lett.* **79**, 1070 (1997).
- [27] K. Kirihara, T. Nagata, K. Kimura, K. Kato, M. Takata, E. Nishibori, and M. Sakata, *Phys. Rev. B* **68**, 014205 (2003).
- [28] T. Rieth and M. Schreiber, *Phys. Rev. B* **51**, 15827 (1995).
- [29] M. Kohmoto and B. Sutherland, *Phys. Rev. Lett.* **56**, 2740 (1986).
- [30] M. Arai, T. Tokihiro, T. Fujiwara, and M. Kohmoto, *Phys. Rev. B* **38**, 1621 (1988).
- [31] A. Koga and H. Tsunetsugu, *Phys. Rev. B* **96**, 214402 (2017).
- [32] F. Flicker, S. H. Simon, and S. A. Parameswaran, *Phys. Rev. X* **10**, 011005 (2020).
- [33] T. Hatakeyama and H. Kamimura, *Solid State Commun.* **62**, 79 (1987).
- [34] H. Aoyama and T. Odagaki, *J. Stat. Phys.* **48**, 503 (1987).
- [35] A. Jagannathan, *Phys. Rev. Lett.* **92**, 047202 (2004).
- [36] A. Chakrabarti, S. N. Karmakar, and R. K. Moitra, *Phys. Rev. B* **39**, 9730 (1989).
- [37] J. Q. You, J. R. Yan, J. X. Zhong, and X. H. Yan, *Europhys. Lett.* **17**, 231 (1992).
- [38] J. You and F. Nori, *J. Phys.: Condens. Matter* **5**, 9431 (1993).
- [39] N. Macé, A. Jagannathan, and F. Piéchon, *Phys. Rev. B* **93**, 205153 (2016).
- [40] N. Macé, A. Jagannathan, P. Kalugin, R. Mosseri, and F. Piéchon, *Phys. Rev. B* **96**, 045138 (2017).
- [41] B. Sutherland, *Phys. Rev. B* **34**, 3904 (1986).
- [42] N. De Bruijn, *Nederl. Akad. Wetensch. Proc. Ser. A* **43**, 53 (1981).
- [43] V. Kumar, D. Sahoo, and G. Athithan, *Phys. Rev. B* **34**, 6924 (1986).
- [44] M. A. Bandres, M. C. Rechtsman, and M. Segev, *Phys. Rev. X* **6**, 011016 (2016).
- [45] H. Huang and F. Liu, *Phys. Rev. B* **98**, 125130 (2018).
- [46] T. A. Loring, *J. Math. Phys.* **60**, 081903 (2019).
- [47] C.-K. Chiu, J. C. Y. Teo, A. P. Schnyder, and S. Ryu, *Rev. Mod. Phys.* **88**, 035005 (2016).